1 Revisiting the tropical Atlantic western boundary circulation
2 from a 25-year time series of satellite altimetry data

3 Djoirka M. Dimoune[1], Florence Birol[2], Fabrice Hernandez[1,2], Fabien Léger[2], Moacyr Araujo[1,3]

4 [1]Laboratorio de Oceanografia Física Estuarina e Costeira (LOFEC), Departamento de
5 Oceanografia da Universidade Federal de Pernambuco (UFPE), Cidade Universitária, Avenida
6 Arquitetura s/n, 50740-550 Recife, PE, Brazil
7 [2]LEGOS, Université de Toulouse, CNES, CNRS, IRD, 18 avenue Edouard Belin, 31400,
8 France
9 [3]Brazilian Research Network on Global Climate Change (Rede CLIMA), Av. dos Astronautas,
10 1758, 01227-010 São José dos Campos, SP, Brazil

11 *Correspondance to:* Djoirka M. Dimoune (pmintodimoune@gmail.com)

12

13 **Abstract.** Geostrophic currents derived from altimetry are used to investigate the surface
14 circulation in the Western Tropical Atlantic over the 1998-2017 period. Using six horizontal
15 sections defined to capture the current branches of the study area, we investigate their respective
16 variations at both seasonal and interannual time-scales as well as the spatial distribution of these
17 variations. Our results show that the central branch of the South Equatorial Current, the North
18 Brazil Current component located south of the equator, the Guyana Current and the northern
19 branch of the South Equatorial Current at 42° W have similar annual cycles, with
20 maxima/minima during boreal winter-spring/October-November. In contrast, the seasonal
21 cycles of the North Brazil Current branch located between the equator and 7-8° N, the North
22 Brazil Current retroflected branch and the North Equatorial Countercurrent show
23 maxima/minima during boreal fall/May. West of 42° W, an eastward current is observed
24 between 0°-2° N, identified as the equatorial extension of the retroflected branch of the North
25 Brazil Current. It is part of a large cyclonic circulation observed between 0°-6° N and 35°-45°
26 W during boreal spring. The North Equatorial Countercurrent shows a two-core structure during
27 the second half of the year, when we also observe the two regions where the North Brazil
28 Current retroflects. The latter can be related to the wind stress curl seasonal changes. At
29 interannual scales, depending on which side of the equator, the North Brazil Current exhibits
30 two opposite scenarios related to the tropical Atlantic Meridional Mode phases. The interannual
31 variability of the North Equatorial Countercurrent and of the northern branch of the South
32 Equatorial Current (in terms of both strength and/or latitudinal shift) at 42° W are also
33 associated to the Atlantic Meridional Mode, while they are associated to the zonal mode phases
34 at 32° W.

35

1   Introduction

The energetic Western Tropical Atlantic (WTA) boundary surface circulation is known to play a key role in the transport of heat, salt and water mass from the southern to the northern hemispheres of the Atlantic Ocean. It corresponds to the return branch of the thermohaline Atlantic Meridional Overturning Circulation (AMOC), influenced by the wind (Schmitz and McCartney, 1993; Schott et al., 2004; Rodrigues et al., 2007). A regional scheme of the surface currents in the study area is proposed in Fig. 1. It is derived from a global analysis of the different works mentioned below.

From 5° S to 15° N, the surface boundary circulation is formed by the North Brazil Current (NBC) flowing northward along the South American shelf. It carries tropical waters originating from the South Atlantic subtropical gyre and contributes to interhemispheric water transport (Johns et al., 1990; 1998; Peterson and Stramma, 1991; Stramma and England, 1999; Fratantoni et al., 2000; Silva et al., 2009; Zheng and Giese, 2009, Garzoli and Matano, 2011). The NBC has its origin near 5° S, with two sources: the central branch of the westward South Equatorial Current (cSEC); and the along-shelf equatorward North Brazil Undercurrent (NBUC) which rises to the surface around 5-6° S (Schott et al., 1998, Dossa et al., 2020). The latter advects warm waters from the South Equatorial Current (SEC) through its southern branch (Schott et al., 1995). Further north, around 5° N, the NBC is also fed by the northern branch of the SEC (nSEC) (Goes et al., 2005). Then, between 5°-9° N and 45-50° W, a large part of the NBC retroflects to form a southeastward retroflected branch (called hereinafter rNBC). Between 3° N and 8° N, this branch first feeds the eastward North Equatorial Countercurrent (NECC) throughout the year, except during the boreal spring. At that time, the NECC is fed only by the North Equatorial current (NEC) (Bourlès et al., 1999a; Goes et al., 2005). The NECC flows eastward between 2° N and 12° N, and crosses the tropical Atlantic (Didden and Schott, 1992; Ffield, 2005; Urbano et al., 2008; Araujo et al., 2017). During the second half of the year, this current shows two cores that can separate into a southern and a northern branch (called sNECC and nNECC, respectively: Urbano et al., 2006; 2008).

At depth, around 3-8° N, Cochrane et al. (1979) and Schott et al. (2004) suggested that, part of the rNBC also feeds the eastward North Equatorial UnderCurrent (NEUC) located around 5° N. In addition, between 2° S and 3° N, the rNBC feeds the subsurface eastward Equatorial UnderCurrent (EUC) (Hisard and Hénin, 1987; Bourlès et al., 1999b; Hazeleger et al., 2003;

67 Hazeleger et de Vries, 2003; Schott et al., 1995; 2004). North of 10° N, the part of the NBC

68 which has not retroflected flows northwestward along the Guyana coast, forming the Guyana

69 Current. The latter is also fed seasonally by the NEC (Johns et al., 1998) and transports warm

70 equatorial waters into the Caribbean Sea (Stramma and Schott, 1999; Garzoli et al., 2003).

71 The WTA boundary surface circulation is wind-driven. In the vorticity equation, the terms that

72 dominate localy are the Ekman pumping and the divergence of the geostrophic currents (Garzoli

73 and Katz, 1983; Urbano et al., 2006). The region is also known to be influenced by large

74 mesoscale activities due to the barotropic instabilities of the currents (Aguedjou et al., 2019;

75 Aroucha et al., 2020). Previous studies of Garzoli and Katz (1983), Jochum and Malanotte-

76 Rizzoli (2003) and Verdy and Jochum (2005) about the WTA boundary circulation and the

77 NECC indicate that, west of 32° W, the Sverdrup balance is no more respected; the advection

78 terms of the relative vorticity due to the eddies and the mean flow become then important. North

79 of the equator, the region is characterized by strong seasonal variability of the wind. The Trade

80 Winds variations influence the current system formed by the NBC, the NBC retroflection

81 (NBCR), the rNBC and the NECC. In particular the NBCR location, the NBC transport and the

82 NECC position/transport respond to the seasonal changes in the wind regimes (Johns et al.,

83 1990; 1998; Garzoli et al., 2003; 2004; Urbano et al., 2006; 2008). This wind influence is

84 traduced by a latitudinal changes of the currents, in conjunction with the Intertropical

85 Convergence Zone (ITCZ) location. The variability of the current strength appears as a regional

86 response of the wind stress curl (WSC) distribution and of the WSC strength over the basin

87 (Johns et al., 1998; Fonseca et al., 2004; Garzoli et al., 2004, Urbano et al., 2006; 2008). In the

88 equatorial region, the EUC seasonal variability is first associated to the basin scale zonal

89 pressure gradient (ZPG), and also to the seasonal cycle of the local wind forcing (Hisard and

90 Hénin, 1987; Provost et al., 2004; Brandt et al., 2006; Hormann and Brandt, 2007; Brandt et

91 al., 2016).

92 The interannual variability of the WTA boundary currents has been little studied because of the

93 lack of long-term data in this area. Nevertheless, Fonseca et al. (2004), using a combination of

94 altimetry and hydrographic data from 1993 to 2000, investigated the influence of the wind on

95 both the NBCR and the NECC variability. They did not find any direct relationship between

96 them. Hormann et al. (2012), used the surface velocity data derived from drifters between 1993

97 and 2009 and highlighted a relationship between the NECC intensity/location and the tropical

98 Atlantic climate modes (ACM), represented by positive and negative phases of the Atlantic

99 zonal mode (AZM) and the Atlantic meridional mode (AMM) (Cabos et al., 2019). In the

100 equatorial Atlantic, Hormann and Brandt (2007) also found such relationship, using a high-
101 resolution ocean general circulation model, observations and sea surface temperature (SST)
102 data. They showed that the EUC transport is affected by the cold and warm events of the AZM
103 (the so called "Atlantic Niño / Niña") and confirmed the previous findings of Goes and Wainer
104 (2003) concerning the link between the interannual variability of the wind and the ACM
105 impacting the strength of the tropical Atlantic circulation.

106 In this study, we propose to revisit the scheme of the WTA boundary surface circulation using
107 a 25-year time series of gridded altimeter-derived geostrophic currents. This dataset is longer
108 than the one used by Fonseca et al. (2004) and allows to provide a more robust description of
109 the current branches described above, as well as of their seasonal and interannual variations.
110 The data also allows to infer regional relationship among these currents. The paper is organized
111 as follow: in Sect. 2, the data and methods used are presented. Section 3 brings some general
112 characteristics of the current variability in the study area. In the fourth section we analyze and
113 discuss the seasonal and spatial variabilities of the surface geostrophic currents and propose an
114 updated seasonal map of the WTA surface circulation. The interannual variability of the
115 circulation is analyzed in Sect. 5. Section 6 is devoted to a general discussion, and Sect. 7 offers
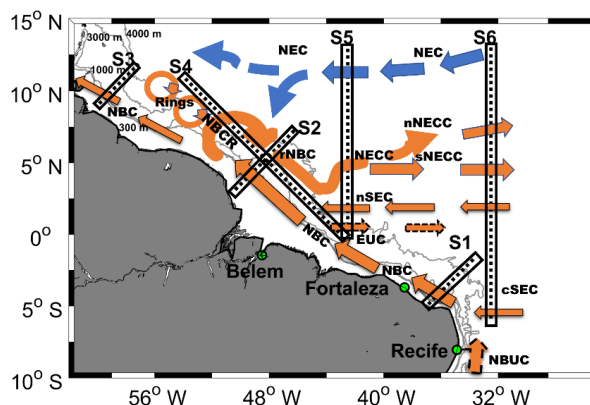116 a summary and some perspectives.

117

118

119

120

121

122

Figure 1. Schematic view of the western boundary surface circulation in the tropical Atlantic derived from Schott et al. (2004), Goês et al. (2005), Urbano et al. (2006; 2008) and Aroucha et al. (2019). The distribution of the horizontal section used to study the different current branches are also indicated in black: S1, S2, S3, S4, S5 and S6. Solid and dashed arrows are the upper and the subsurface currents, respectively. The blue and orange colors of the arrows show connections with the northern and southern hemisphere waters, respectively. From south to north, the currents shown are the North Brazil Undercurrent (NBUC), the central and northern branches of the South Equatorial Current (cSEC and nSEC, respectively), the North Brazil Current, its retroflection and its retroflected branch (NBC, NBCR and rNBC, respectively), the Equatorial Undercurrent (EUC), the North Equatorial Countercurrent (NECC) and its southern and northern branches (sNECC and nNECC, respectively), and the North Equatorial Current (NEC). The 300 m, 1000 m, 3000 m and 4000 m isobaths (grey lines) are from the ETOPO2v1 database.

2 Data and methods

2.1 Altimeter-derived geostrophic currents

From along-track altimetry sea surface height measurements of all available satellite missions, the Copernicus Marine Environment Monitoring Service (CMEMS) produces daily maps of ocean dynamic topography, and derives then geostrophic surface currents. Here, we use the SEALEVEL_GLO_PHY_L4_REP_OBSERVATIONS_008_047 product (https://resources.marine.copernicus.eu/) from January 1993 to December 2017. Daily maps of dynamic topography are estimated by optimal interpolation on $0.25° \times 0.25°$ global grid (details can be found in Pujol et al., 2016), and the geostrophic currents are computed using the 9-points stencil width methodology (Arbic et al., 2012) for latitudes outside the equatorial band (Equator $\pm5°$) and the β-plane approximation (Lagerloef et al., 1999) in the equatorial band.

For the present work, focusing on the seasonal and interannual variability, the daily gridded velocity fields from CMEMS have been averaged on a monthly basis. Note that we have removed data located in the Amazon region because they show unrealistic values, probably due to erroneous altimetry measurements which have not been correctly flagged. We have then defined six horizontal sections (called S1, S2, S3, S4, S5 and S6, respectively), so that they cross perpendicularly at least one of the regional current branches (see Fig. 1). For each section, the original zonal and meridional surface velocity components have been rotated in order to derive the along-section and cross-section velocity components. In this study, we considered only the cross-section component.

2.2 Ekman currents

We also used the GEKCO product (Geostrophic and Ekman Current Observatory, Sudre et al., 2013), made available by LEGOS (Laboratoire d'Etudes en Géophysique et Océanographie Spatiale). It provides the zonal and meridional components of the daily wind-driven currents at a 0.25° resolution. The latter were calculated using the standard Ekman formulation, and the estimates have been improved in the equatorial region. Then, they were validated with independent observations from both Lagragian and Eulerienne perspectives (see Sudre et al. 2013 for more details). For this work, the daily current estimates have been monthly averaged over the period 1993-2017.

2.3 Wind velocity

Monthly wind velocity fields from the ERA5 atmospheric reanalysis produced by the European Centre for Medium-Range Weather Forecasts (ECMWF, http://www.ecmwf.int) are used in

178   order to evaluate the influence of the remote winds on the WTA ocean circulation. They were

179   downloaded from the Copernicus Climate Change data server over the January 1993 -

180   December 2017 period. We used the wind velocity data to calculate the wind stress field as

181   follows.

182   The zonal and meridional components of the wind stress, ζ_x and ζ_y are calculated using empirical

183   formulations (Large and Pound; 1981: Gill, 1982; Trenberth et al., 1990) following NRSC

184   (2013):

185                               $\zeta_x = \rho_{air} C_D W * U$ (1)

186                               $\zeta_y = \rho_{air} C_D W * V$ (2)

187   where U/V represent the zonal/meridional wind velocity components; W, the wind speed

188   amplitude; ρ_{air}, the air density (1.2 kg m^{-2}); C_D, the drag coefficient at the ocean surface,

189   calculated according to Large and Pound (1981).

190   The wind stress curl (WSC) is then deduced following Gill (1982):

191
$$Curl(\zeta) = \frac{\partial \zeta y}{\partial x} - \frac{d\zeta x}{dy}$$ (3)
192

193   From the WSC estimates, we compute the ITCZ location (~zero values location), the

194   minimum/maximum of the negative/positive values, and the WSC strength (sum of the absolute

195   minimum negative value and the absolute maximum positive value) in the tropical Atlantic.

196   Each of these parameters is zonally averaged over the region covering 6° S -16° N, and 30° W-

197   0° W, following Fonseca et al. (2004).

198   **2.4   Sea Surface temperature**

199   Monthly estimates of Sea Surface temperature (SST) are also used in order to compute the

200   Atlantic climate mode indexes and evaluate their possible relationship with the interannual

201   changes observed in the WTA boundary circulation. A global gridded SST product, with a 1°

202   spatial   resolution   is   downloaded   from   the   NOAA   repository

203   (https://www.esrl.noaa.gov/psd/gridded/data.noaa.oisst.v2.html, Reynolds et al. 2002).

204   The AZM index is calculated considering the SST anomalies (SSTA) relative to the 1993-2017

205   monthly climatology in the ATL3 region bounded by 3° S-3° N/20° W-0° E (Zebiak, 1993,

206   Hormann et al., 2012). The AMM index is also based on SSTA relative to the 1993-2017

207   monthly climatology, and calculated as the difference between the spatial average SSTA in the

208   box 5° N-25° N/60° W-20° W and the spatial average SSTA in the box 20° S-5° N/30° W-10°

209   E (Servain, 1991; Hormann et al., 2012).

3   General characteristics of the circulation in the Western Tropical Atlantic

211   The mean WTA surface geostrophic circulation is first derived by averaging the gridded

212   altimetry current maps over 1993-2017 (Fig. 2a). We distinguish three different areas. From

213   south/east to north/west:

214   1) The NBC formation area starting around 5°S: the westward cSEC flowing north of 6°S

215   (mean value of ~ 0.3 m s^{-1}) feeds the NBC-NBUC current system around 34°-36° W.

216   The NBC amplitude increases along its northward along-shelf course, up to 0.8 m s^{-1}

217   around 3° S. Then it slows down toward the equator, before increasing again north of

218   3° N. Along the Guyana coast, its mean velocities are again weaker, with values of ~

219   0.3 m s^{-1}.

220   2) The NBC retroflection region between 5°-8° N: in this area, the NBC undergoes an

221   eastward recirculation, which feeds a southeastward vein of current so-called the NBC

222   retroflected branch (rNBC). The rNBC reaches annual mean velocities of ~0.6 m s^{-1}.

223   3) The area located between 3°-6° N and 42°-46° W: it represents the region where the

224   rNBC meanders with an annual mean velocity of 0.5 m s^{-1} to partly feed the surface

225   eastward NECC which decays along its course. This area is located in the region of high

226   wind variability (Figure not shown).

227   In addition, we also observe the westward nSEC flowing between 2°-6° N, with stronger

228   velocity values at the eastern part of the basin (mean velocity larger than 0.3 m s^{-1}).

229   We computed the mean power spectral density of the daily geostrophic current time series in

230   order to detect the dominant components of the WTA current variations (not shown). It

231   highlighted three main energy zones:

232   1) at intraseasonal scales with different peaks at periods less than 120 days,

233   2) at seasonal scale,

234   3) at interannual timescale, with peaks at periods larger than 600 days.

235   We filtered the velocity time series using different cutoff frequencies in order to isolate each of

236   this component of the current variability: below 120 days, between 120 days and 600 days and

237   above 600 days. Then, we computed the ratio between the standard deviation of each filtered

238   current field and of the total current field. The resulting maps (Fig. 2b-d) show the relative

239   importance of each component with regard to the total variance, as a function of the location.

240   We observe the predominance of the seasonal variability in the whole WTA (overall ratio of

241   0.44), with the highest values (0.48) observed along the continental shelf, in the NBC region,

242   and between 0°-2° S east of 36° W. Intraseasonal fluctuations are also important in the same

243   areas (with largest ratio of 0.44) while the interannual variability is only noticeable north/east

244   of 4° N/40° W, where the NECC is located, with values representing less than 0.2 of the total

245   variance (consistent with Richardson and Walsh, 1986). In this study, we focus on the seasonal

246   and interannual timescales.

247

248

249

250

251

252

253

254

255

256

257
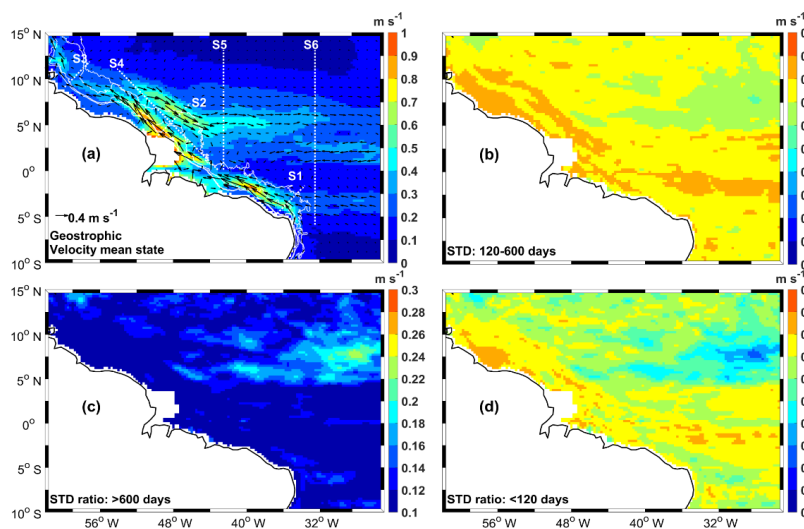
Figure 2. (a) Temporal mean of the geostrophic currents (amplitude in m s^{-1} and vectors) in the study area between 1993 to 2017; **(b), (c)** and **(d)** ratios between the standard deviations of the currents for the signals between 120 and 600 days, more than 600 days and less than 120days, respectively, and the standard deviation of the total currents. The white dashed lines S1, S2, S3, S4, S5, S6 in **(a)** represent the cross-sections of the currents, and the solid white lines are the 300 m, 1000 m, 3000 m and 4000 m isobaths.

258
259
260
261
262
263
264
265
266
267
268
269
270
271
272
273
274
275
276
277

278   Then we monthly averaged the daily geostrophic currents and extracted the cross-section

279   geostrophic velocities along the six sections defined above (Fig. 1). In order to remove the

280   intraseasonal variability, the monthly velocity estimates are further low-pass filtered using a 4-

281   month cutoff frequency. The time-space diagrams (also called Hovmöller diagrams) along the

282   six sections are plotted in Fig. 3. We can clearly observe large changes in both time and space

283   with respect to the different current branches, illustrating the complexity of the surface

284   circulation in the WTA. The seasonal and, in a lesser extent, the interannual current fluctuations

285   mentioned above are clearly visible in the different sections. For each of them, the time-average

286   current values are also computed as a function of the latitude (left-side plots in Fig. 3),

287   highlighting the mean spatial extension of the current veins crossing the corresponding section.

288   Note that in addition to the main currents mentioned in Fig. 1, between 1.5° S-2° N, the sections

289   4 to 6 show an eastward current, positioned where the EUC might be located. At 44° W, Bourlès

290   et al. (1999b) have also noticed the presence of a surface eastward flow above the EUC, which

291   was identified to be different than the EUC. So, we chose to name it X hereinafter in order to

292   further investigate this signal and its origin.

293   Table 1 summarizes the mean current width derived along the different sections (using left-side

294   plots in Fig. 3). Note first that a positive current convention is chosen for the sections as follows:

295   northward NBC along sections 1 to 3; eastward NBCR along section 4; eastward NECC along

296   sections 5 and 6, and eastward X flows along sections 4 to 6. Hence, the signatures of the rNBC

297   on the section 2, the nSEC (sections 4 to 6) and the cSEC (section 6) are considered as negative.

298   From Table 1, we observe that the NBC becomes narrower from the section 1 to the section 2.

299   The retroflection zone (section S4, Fig. 3S4) extends from 3.7° N to 10.5° N, in agreement with

300   Fonseca et al., (2004) who found the northernmost position of the NBCR around 11° N. North

301   of the retroflection, the NBC along the Guyana coast is weaker, but broader relatively to the

302   section 2 (NBC2 and NBC3 in Fig. 3). From section 6 to 4, the nSEC signature changes. It is

303   wider at 32° W (nSEC6), then narrower at 42° W (nSEC5), and widens again closer to the shelf

304   at 44° W (nSEC4) (respectively 550, 67 and 190 km in Table 1). The NECC extension also

305   varies from 32° W to 42° W, and is wider and located further north on the east, with a mean

306   width extending from 860 km (NECC5) to 920 km (NECC6).

307

308

309

310 **Table 1.** Extension in latitude and km of the different currents branches crossing the different sections: NBC1,

311 NBC2 and NBC3 are respectively the North Brazil Current captured on sections 1, 2 and 3; NECC5 and NECC6

312 are respectively the North Equatorial Countercurrent on the sections 5 and 6; nSEC4, nSEC5 and nSEC6 are

313 respectively the northern branch of the South Equatorial Current (SEC) on the sections 4, 5 and 6; cSEC6 is the

314 central branch of the SEC on the section 6; and X4, X5 and X6 are the equatorial eastward flow X on respectively

315 on the sections 4, 5 and 6.

List of current veins	Latitudinal coverage	Current width (km)
NBC1	1.3° S-4.6° S	~ 520
NBC2	3.6° N-5° N	~ 220
rNBC2	5° N-7.4° N	~ 380
NBC3	9.1° N-11.9° N	~ 440
NBCR4	3.7° N-10.5° N	~ 760
nSEC4	2° N-3.7° N	~ 190
X4	1.2° N-2° N	~ 120
NECC5	2.4° N-10.1° N	~ 860
nSEC5	1.7° N-2.3° N	~ 70
X5	0° N-1.7° N	~ 190
NECC6	4.1° N-12.4° N	~ 920
nSEC6	0° N-4.1° N	~ 550
X6	0° S-1.4° S	~ 110
cSEC6	1.4° S-5.9° S	~ 500

316

317

318

319

320

321

322

323

324

325

326

327

328

329

330

331

332

333

334

335

336
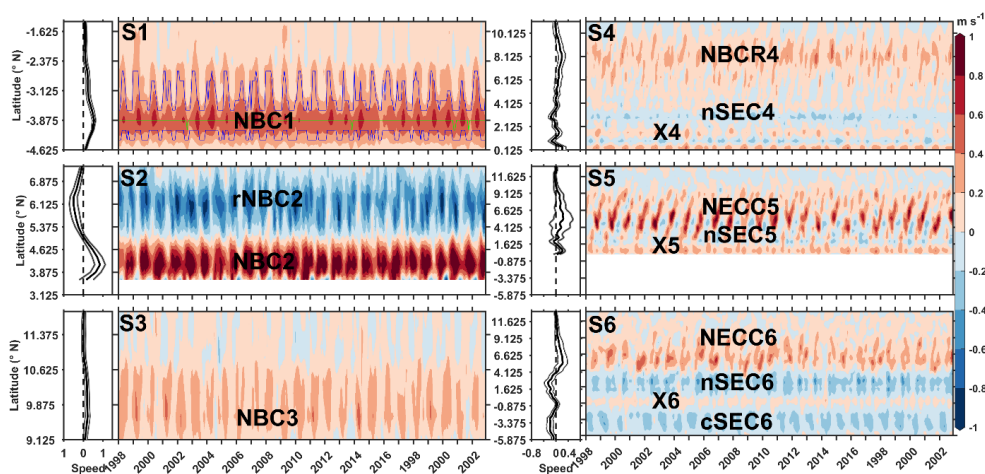
Figure 3. Hovmöller diagrams (1993 to 2017) of the cross-section current components (m s^{-1}) for S1, S2, S3 S4 S5 and S6. At the left of each diagram, the time series of time averages of the cross-section current (thick lines), framed by their corresponding standard deviations (thin lines) are plotted as a function of latitude. The red (blue) colors show the northward/eastward (southward/westward) directions of the cross-currents: North Brazil current (NBC), its retroflected branch (rNBC) and the retroflection signature at the limit between the NBC and the rNBC (NBCR); North Equatorial Countercurrent (NECC); the equatorial surface eastward flow named X; northern and the central branches of the South Equatorial Current (nSEC and cSEC, respectively). The numbers next to the acronym of the currents represents the number of the section. The green line in S1 indicates the time series of the maximum velocity of the cross-section current (NBC), and is framed by the time series of the maximum velocities divided by 2 (blue lines) over 1993-2017 period.

363   In order to further investigate the temporal variations of the current amplitude, the maximum

364   velocity values of each current vein identified in Table 1 have been extracted for each month

365   (corresponds to the current core and called Vmax hereafter: see Fig. 3, green line on S1). The

366   location of Vmax corresponds to the location of the current core. Then the corresponding

367   current width is estimated, considering the part of the section where the velocity is larger than

368   Vmax/2 (see Fig. 3, blue lines on S1). Finally, the relative intensity is computed by averaging

369   the cross-section velocity values over the estimated current width. For each current vein

370   crossing the six sections (Left column of Table 1), we compute the monthly time series of the

371   resulting Vmax, current width and relative current intensity/strength. Note that the latter has

372   also been computed by averaging velocity values over the full transect of each current vein

373   (e.g., not only where the velocity is larger than Vmax/2), but the results did not correctly reflect

374   the current variability observed in Fig. 3 and Fig. 4 (not shown). For the NBCR and the NECC,

375   the variability of the maximum velocity of two flow branches and their corresponding locations

376   is also analyzed, in order to compare with the study of Fonseca et al. (2004). It will also be used

377   to investigate the variability of the current location with respect to the wind variability and to

378   the tropical Atlantic climate modes. In this study, the presence of two branches of the e NBCR

379   and the NECC two-core structure are identified when the flow velocity profile shows two local

380   maxima separated by a local minimum respectively, in the NBCR region (considered between

381   4°-10° N) and the NECC region (considered between 3°-11° N) (Fig. 4S4-S6).

382

383

384

385
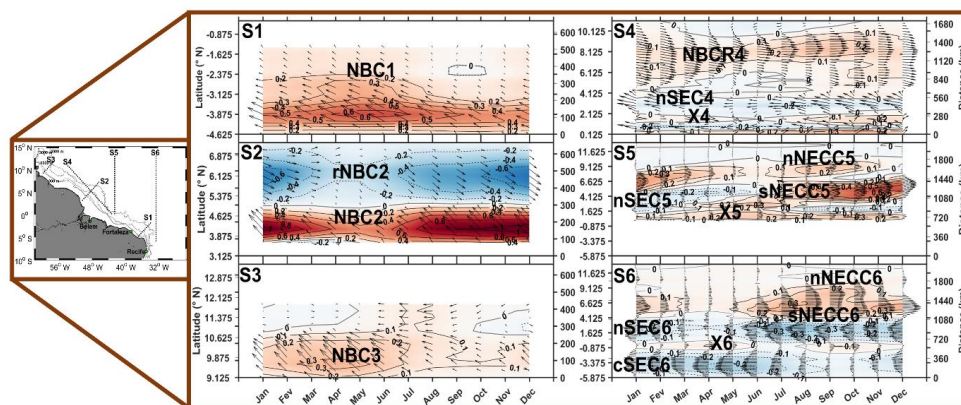
Figure 4. Hovmöller diagrams of the monthly climatology of the surface geostrophic (vectors superimposed on amplitude in m s^{-1}) over the 1993-2017 period. S1, S2, S3, S4, S5 and S6 are respectively for the sections 1 to 6 represented over the study area (Left map). nNECC and sNECC are respectively, the northern and southern branches of the North equatorial Countercurrent (NECC); NBC, the North Brazil Current; NBCR, the NBC retroflection limit; rNBC, the retroflected branch of the NBC, nSEC and cSEC, the northern and the central branches of the South Equatorial Current, respectively; and X, the equatorial surface eastward flow. On the right sides of each diagram, the distances from the lowest point (in km) are indicated.

4   Seasonal variability

Here we focus on the seasonal cycle of the different current branches observed in the study
area. Therefore, a monthly climatology of the velocity estimates shown in Fig. 3 is calculated
for each of the six sections (Fig. 4). For further analysis, the monthly climatology of Vmax,
Vmax location, the current width and the relative current intensity has also been derived from
the corresponding monthly time series for different current components ((Fig. 5). Below, we
analyze the results from the southeast to the northwest of the study area.
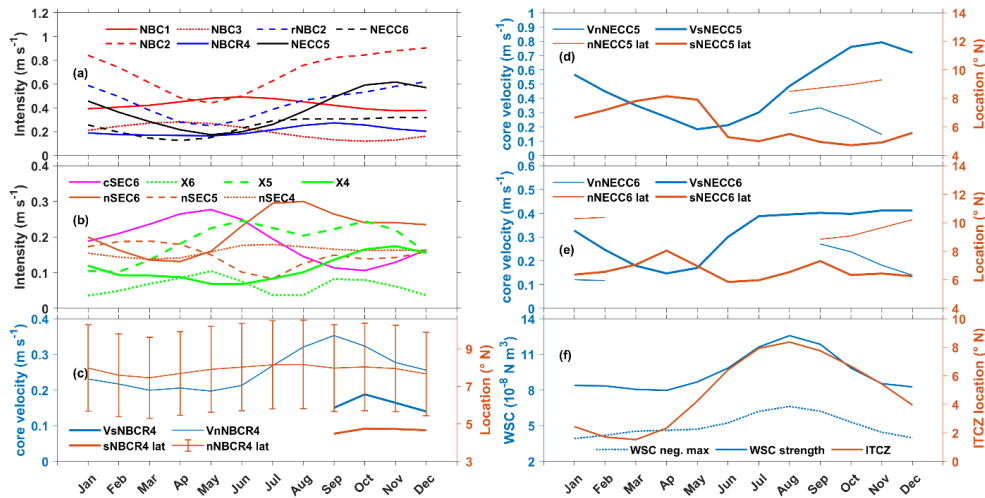
Figure 5. Monthly climatology of: the relative currents' intensity (m s^{-1}) **(a-b)**; the cores velocity/location in the North Brazil Current Retroflection (NBCR) regions **(c)**; the cores velocity/location of the North Equatorial Countercurrent (NECC) branches along sections 5 and 6 **(d-e)**; and the absolute values of the maximum negative wind stress curl (WSC neg. max), the WSC strength and the ITCZ location **(f)**. **(a)**: NBC1, NBC2 and NBC3 represents the North Brazil Current (NBC) on the crossing sections 1, 2 and 3, respectively; rNBC2 represents the retroflected NBC branch (rNBC) crossing section 2; NBCR4, represents the NBCR flow crossing section 4; NECC5 and NECC6 represent the NECC crossing 5 and 6, respectively. **(b)** nSEC4, nSEC5 and nSEC6 represent the northern branch of the South Equatorial Current (SEC) crossing sections 4, 5 and 6, respectively; cSEC6 represents the central branch of the SEC crossing section 6; and X4, X5 and X6 represent the equatorial surface eastward flow X crossing sections 4, 5 and 6, respectively. On **(c)**, **(d)** and **(e)**, the "V" initials/lat" at the end of each acronym represent the core velocity/location (blue/orange color). The nNBCR/sNBCR and nNECC/sNECC represent the northern/southern core in the NBCR and the NECC regions, respectively.

4.1 The North Brazil Current and its retroflection

In Fig. 4, the NBC (Section 1) and the cSEC (Section 6) are observed both located at ~ 4° S and present similar seasonal cycles, with stronger flows during the first half of the year. The cSEC6 velocity maximum (0.3 m s^{-1}) / minimum (0.1 m s^{-1}) appears in May/October, respectively. The NBC1 velocity maximum (0.6 m s^{-1}) / minimum (0.4 m s^{-1}) appears in May-June/November-December (Fig. 5a). These annual cycles are also similar to the annual cycle of the NBUC transport observed by Rodrigues et al. (2007) at 10° S and which is related to the bifurcation location of the sSEC. This suggests that at its southernmost location, the seasonal variability of the NBC might be partly driven by the location of the sSEC bifurcation, which has been shown to be influenced by the annual cycle of the WSC over the area 5°–10° S, 25°–40° W (Rodrigues et al., 2007).

When comparing the NBC along sections S1, S2, S3 and S4 (Fig. 4S1-S4 and Fig. 5), it clearly depicts two different seasonal cycles along its northward path. The NBC2, NBCR4 and the rNBC2 flows show approximately the same seasonal cycles, in opposite phase with NBC1 and NBC3 ones, approximatively in phase. NBC2 is narrower but relatively stronger than NBC1. It decreases from January to May (by ~ 0.4 m s^{-1}), and then increases again to reach a maximum in November-December (1 m s^{-1}). Compared to NBC2, the rNBC2 is broader (width of ~ 350 km against 200 km) but less intense (maximum of 0.6 m s^{-1} in November-December). In Fig. 4, from September to January, we observe two retroflections of the NBC: the main one around 8°N and a secondary one to the south, between 4-6° N (Fig. 4S4 and 5c). The flow of this secondary retroflection (called sNBCR) reaches its maximum intensity in October while the main retroflection flow (called nNBCR) reaches its maximum one month earlier. Then, it migrates northward to join the nNBCR4; and both are completely merged at the beginning of the following year (Fig. 4S4). Both branches merge at the beginning of the year and the NBCR then weakens to reach its minimum intensity in May. Note that the seasonal cycles of the NBC2 and the NBCR have are similar to the one of the NBC transport obtained by Johns et al. (1998) and Garzoli et al. (2004) using acoustic Doppler current profilers (ADCP)/Inverted Echos sounders/Pressure gauge data. Johns et al. (1998) related the seasonal cycle of the NBC observed in this area to the remote wind stress curl forcing across the tropical Atlantic. Here, we also see that the seasonal cycles of the NBC branches north of the equator (except the NBC continuity along the Guyana coast) follow the remote wind stress curl strength by one to four months (Fig. 5a-f). The northernmost location of the nNBCR maximum intensity occurs in August, when the maximum WSC strength is reached (Fig. 5c, f). The root mean square (rms)

481   of the monthly mean values of its location (Fig. 5c) is nearly constant (~2.3°), and is consistent

482   with the evidence that there may not be a preferred season for NBC ring formation (Garzoli et

483   al., 2003; Goni and Johns, 2003).

484   Further north, the NBC component flowing along the Guyana coast (NBC3) is twice wider (~

485   440 km) and less intense than the NBC2 (Fig. 4S2-S3). It reaches a minimum in October (~ 0.1

486   m s^{-1}), and a maximum during March-May (0.3 m s^{-1}) when the NBCR4 is minimum (Fig. 4S3-

487   S4 and 5). As already mentioned, its seasonal cycle is similar to the NBC1 and cSEC, and might

488   also be influenced by the sSEC bifurcation location.

489   **4.2   The North Equatorial CounterCurrent**

490   The NECC (both NECC5 and NECC6) seasonal cycle is similar to the ones of the NBC2,

491   NBCR4 and rNBC2 (Fig. 4S2, S4, S5-S6). It weakens along its pathway and its intensity is

492   maximum in November-December (~ 0.6 m s^{-1} at 42° W and ~ 0.3 m s^{-1} at 32° W), and

493   minimum in April-May (Fig. 5a). During the second part of the year, we observe the two-core

494   structure previously investigated by Urbano et al. (2006; 2008). The two cores/branches are

495   seen first at 42° W in August, then at 32° W in September (Fig. 4 and 5d-e). The northern

496   branch (nNECC) is narrower (located between 7°-9° N) and stronger (0.3 m s^{-1}) in August-

497   September at 42° W (Fig. 4S5 and 5d). It is even separated from the southern branch from

498   October to December. At 32° W, the NECC appears with one single core from September

499   (northern core velocity of ~ 0.2 m s^{-1}) to November. The northern core is gradually decreasing

500   in intensity and shifting northward until forming a separated second branch, which is located

501   between 9-11° N from December to February, and then becomes very weak in March-April

502   (Fig. 4S5 and 5e). From June to July, the NECC signature (sNECC branch) is located between

503   3-4° N at 42° W, and is connected from the south to the eastward flow associated with X5 in

504   Fig. 4S5. Urbano et al. (2008) showed with ADCP data at 38° W that the eastward flow south

505   of the NECC corresponds to the mixing of NEUC and EUC waters during this period of the

506   year. The presence of the equatorial surface eastward flow X5 suggests that this latter may be

507   the one that favors the surfacing and the connection of both currents during June-July. From

508   June to November, the sNECC branch increases simultaneously with the rNBCR2. However, it

509   reaches its maximum one month earlier (November) and start decreasing when the rNBC is still

510   increasing. This confirms that the NECC is not only fed by the rNBC at the surface as suggested

511   by Verdy and Jochum, 2005. The sNECC witnesses the same variability at both 32° W and 42°

512   W, but reaches its minimum early in March-April at 32° W when the climatological NECC is

513   described in the literature as a reversing flow or is missing at its usual location (Garzoli and

514   Katz, 1983; Garzoli, 1992). At this location (32° W), the sNECC starts increasing from April-

515   May, between 4°-6° N far from the eastward flow X, and grows until November. Burmeister et

516   al. (2019) showed that, in the central Atlantic, when the ITCZ migrates northward (April to

517   August) (Fig. 5f), the nSEC recirculated eastward to reach the NEUC which then increases. The

518   presence of the sNECC flow in April-May may suggest that the NECC flow might be initiated

519   by the recirculation of the nSEC which should mix with the upper NEUC water during this

520   period. It reaches its first maximum in July-August together with the nSEC, and a second

521   maximum in November (Fig. 5a, b, e). At 32° W and 42° W the sNECC shows two northward

522   migrations. The first migration occurs from June-July (June) to August (September) at 42° W

523   (32° W), and the second occurs from October to April (Fig. 5d-e). Fonseca et al. (2004) also

524   found such behaviors but with some differences: two northernmost NECC locations in February

525   and August, and two southernmost NECC locations in June and December. But they lacked

526   data between March and May, and we do not use the same methods to compute the core

527   position.

4.3   The central and northern branches of the South Equatorial Current

529   Although the cSEC and nSEC are two branches of the westward SEC flow, they do not have

530   the same seasonal cycle (Fig. 4S4, S5, S6). The cycles of the nSEC4, nSEC5 and nSEC6 have

531   maxima at different periods of time. At 32° W, the nSEC (nSEC6) increases from April to reach

532   a maximum of ~ 0.3 m s^{-1} in August, following the migration of the ITCZ (Fig. 5b, f). During

533   this time, at 42° W, the nSEC (nSEC5) migrates northward, and its intensity decreases until

534   July, when it almost disappears. The eastward flow X then appears (Fig. 4S5). The nSEC5 is

535   observed again after July, increases and reach a maximum of ~ 0.2 m s^{-1} in March (Fig. 4S5,

536   S6 and Fig. 5b). Over the continental shelf, most of the nSEC joins the NBC (section 4, around

537   2-4° N and 46° W) and a part of the flow deviates southeastward to join the rNBC and form the

538   eastward flow X4 (captured along section 4, Fig.4S4). The nSEC component that joins the NBC

539   reaches its maximum of ~ 0.2 m s^{-1} between June and August (also following the ITCZ

540   northward migration, Fig. 5b, f). However, the nSEC seasonal variations are relatively small (~

541   0.15 m s^{-1}) (Fig. 4S4). It is particularly true for nSEC4 but the angle of the section relative to

542   the flow probably leads to a significant reduction of the current amplitude captured.

4.4   The eastward current X

544   Figure 4S4-S6 shows the presence of an eastward current near the equator. Such feature was

545   already observed and mentioned by Hisard and Hénin (1987) and Bourles et al. (1999b) using

546   hydrographic and ADCP data. In Fig. 4S4, eastward flows are captured between 1-2° N (X4)

20

547   and along the equator. As mentioned in Sect. 4.3, they may be composed of the part of the nSEC

548   that does not join the NBC and the rNBC (which is kwown to feed the EUC in the thermocline

549   layer). The weaker intensity of X4, compared to X5 (i.e. X at 42) is explained by the angle

550   between S4 and the current direction. But the weaker intensity of X6 (i.e. X at 32° W) is due to

551   the weakening of the corresponding eastward flow between both longitudes. X4 and X5 are

552   observed almost throughout the year (Fig. 4S4-S6) and their amplitude follows a semi-annual

553   cycle (Fig. 5b) similar to the EUC in the eastern Atlantic (Hormann et al. 2007). However, the

554   periods of the maxima are slightly different from location to another. X4 displays a semi-annual

555   cycle, with a weak maximum in March-April (~ 0.1 m s^{-1}) and another maximum in November

556   (~ 0.2 m s^{-1}). X5 amplitude is larger because of the merging of X4 with the eastward flow seen

557   along the equator (Fig. 4S5). Its maxima occur in June and October with similar intensity (more

558   than 0.2 m s^{-1}) (Fig. 5b). X6 (at 32° W) is weaker, but reaches its maxima in May and

559   September-October (less than 0.1 m s^{-1}). Since this eastward X flow is almost not documented

560   in the literature, we will come back to it in Sect. 6.

561   **5   Interannual variability**

562   Beyond the dominant seasonal variability of the circulation at regional scale, we also observe a

563   year-to-year variability of the surface velocities in the study area (Fig. 2 and Fig. 3). The latter

564   is analyzed here, using the time series of the characteristics of the different current branches

565   (see end of Sect. 3) captured along the 6 sections (Fig. 6). We will also analyze this variability

566   in the light of the tropical Atlantic climate modes.

567
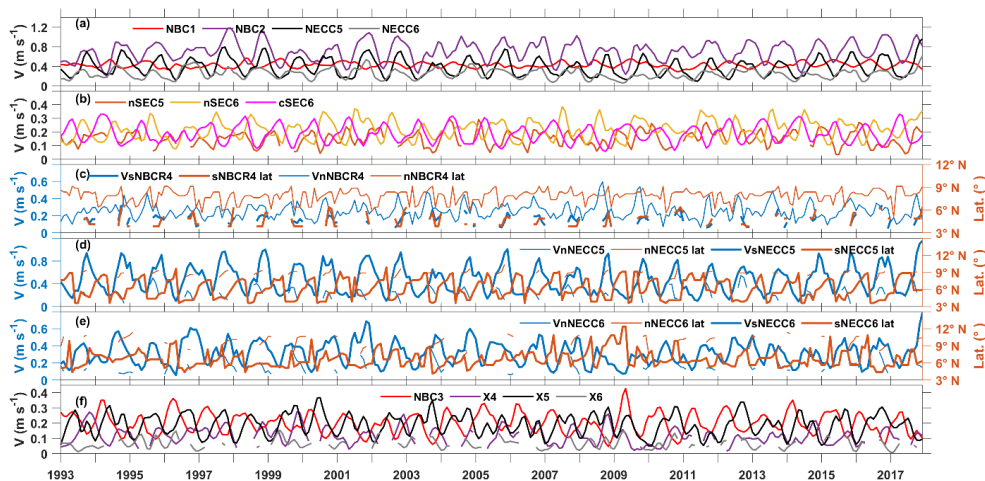
Figure 6. Time series of the 4-month low-pass filtered characteristics of the geostrophic currents **(a-f)** captured along sections 1 to 6. **(a)**: intensity of NBC crossing the sections 1 (NBC1) and 2 (NBC2), and of the NECC crossing the sections 5 (NECC5) and 6 (NECC6). **(b)**: intensity of the cSEC crossing the section 6 (cSEC6) and of the nSEC crossing the sections 5 (nSEC6) and 6 (nSEC6). **(c)**, **(d)** and **(e)** core velocities and the locations of the northern and southern cores of respectively the NBCR flows crossing the section 4 (NBCR4), and of the NECC cores on sections 5 (NECC5) and 6 (NECC6). **(f)** NBC crossing the section 3 towards the Guyana coast (NBC3) and the equatorial surface eastward flow crossing the sections 4 (X4), 5 (X5) and 6 (X6). The "V" initials at the beginning, and "lat" at the end of each acronym of the legends in **(c)**, **(d)** and **(e)** represent the core velocity and location, respectively (blue and orange colors, respectively). The thin (tick) lines represent the northern (southern) branches of these currents/flows.

22

589   In Fig. 6a-b we observe that over the whole study period the intensities of the cSEC6 (cSEC

590   along section 6) and of the NBC1 (NBC along section 1) and NBC2 (NBC along section 2)

591   vary between 0.05-0.35 m s^{-1}, 0.3-0.6 m s^{-1} and 0.2-1.2 m s^{-1}, respectively. with corresponding

592   mean values of 0.2 m s^{-1} ± 0.06, 0.4 m s^{-1} ± 0.06 and 0.7 m s^{-1} ± 0.2. To the north, when crossing

593   section 3, the NBC weakens and ranges between 0.05-0.43 m s^{-1} with a mean intensity of 0.2

594   m s^{-1} ± 0.07. In the equatorial region (±5° of latitude), along sections 5/6, the nSEC intensity

595   varies between 0.05-0.3 m s^{-1}/0.1-0.4 m s^{-1}, with a mean value of 0.15 m s^{-1} ± 0.05/0.2 m s^{-1} ±

596   0.07 (Fig. 6b). The eastward flow X intensity vary between 0.15-0.3 m s^{-1}, 0.05-0.4 m s^{-1} and

597   0-0.15 m s^{-1} when crossing sections 4, 5 and 6, respectively, with corresponding mean values

598   of 0.12 m s^{-1} ± 0.05, 0.2 m s^{-1} ± 0.07, and 0.06 m s^{-1} ± 0.03.

599   As mentioned in Sect. 3, the interannual variability is more important in the eastern part of the

600   basin, and especially in the NECC region. The two-core structure of the NECC and the NBCR

601   regions show the highest year-to-year variations in both velocity and location (Fig. 6c-e). The

602   NECC/NBCR time series were found significantly correlated (>0.98) in terms of both intensity

603   and core velocity (sNECC and nNBCR; Figure not shown). At 42° W, the sNECC/nNECC)

604   velocity core varies between 0.1-1.2 m s^{-1}/0.05-0.55 m s^{-1}, with a mean value of 0.5 m s^{-1} ± 0.25

605   /0.25 m s^{-1} ± 0.1. It is located between 3.6°-9.9° N/7.6°-10.4° N, with a mean location at 6.1°

606   N ± 1.7°/8.9° N ± 0.8° (Fig. 6d). At 32° W, it varies between 0.05-0.8 m s^{-1}/0.05-0.5 m s^{-1}, with

607   a mean velocity of 0.3 m s^{-1} ± 0.13/0.2 m s^{-1} ± 0.09. It is then located between 4.1°-12.4° N/7.4°-

608   11.6° N, with a mean location of 6.6° N ± 1.4°/9.7° N ± 1.1° (Fig. 7e). The sNBCR /nNBCR

609   maximum velocity crossing the section 4 varies between 0.05-0.3 m s^{-1}/0.05-0.6 m s^{-1}, with a

610   mean value of ~ 0.15 m s^{-1} ± 0.06/0.25 m s^{-1} ± 0.08. It is located between 3.9°-6.4° N / 5.1°-

611   9.1° N, with a mean location of 4.7° N ± 0.8°/7.9° N ± 0.8°. Northeast of the equator, for all

612   these current branches, we observe important year-to-year variations, both in terms of current

613   core location and of velocity amplitude.

614   For further analysis, the anomalies of the current's characteristics (intensity and core

615   value/location) relative to their monthly climatology have been computed (Fig. 7). First, we do

616   not see obvious relationship between the different resulting monthly anomaly time series over

617   the whole period investigated. No relationship was found between the evolution of the NECC

618   branches intensity/core value and their location, or the NBCR flows maximum velocity and

619   their location. However, for some particular years, both the NECC intensity/core velocity and

620   location show significant anomalies at 32° W. For example, the monthly anomalies of the

621   sNECC6 location were shifted far to the north / south in 2009 and 2010 / 1996 and 2001.

23

622   Simultaneously, the monthly anomalies of the sNECC6 intensity/core value were unusually

623   weak / strong (Fig. 7f-g).

624   To investigate the relationship between the AMM, the AZM, and the characteristics of the

625   different current branches between 1993 and 2007, we computed the three-month running mean

626   of both the monthly anomaly time series and of the climate mode indexes (so-called 3-month

627   anomaly time series). The latter have been correlated with each other in order to learn more

628   about the spatio-temporal characteristics of the interannual variability in the study area (Figures

629   not shown). Only the correlations greater than ±0.5 and which have been found significant with

630   95 % of confidence level, performing the Student test are discussed below (listed in Table 2).

631

632

633

634

635

636

637

638

639

640

641

642

643

644

645

646

647
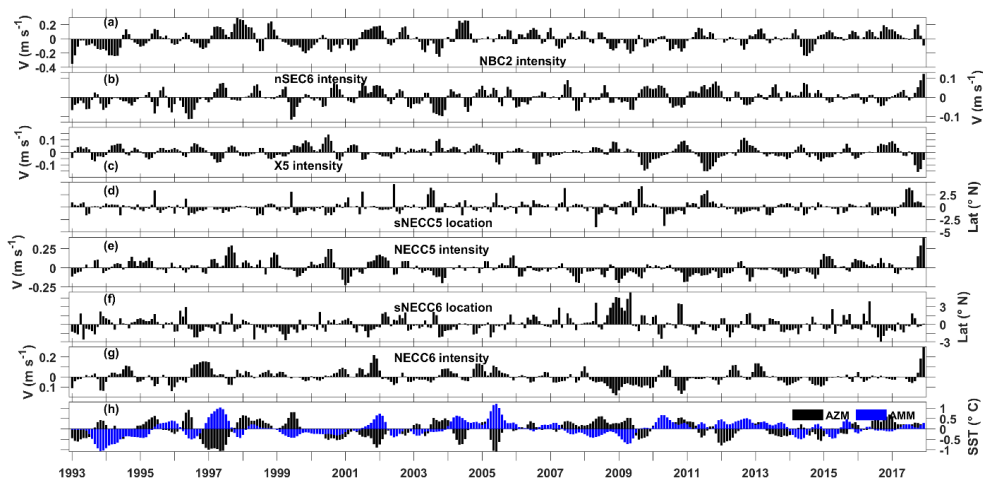
Figure 7. Time series of monthly anomalies relative to the monthly climatology for: **(a)**, the NBC intensity on the section 2; **(b)**, the nSEC intensity on the section 6; **(c)**, the equatorial surface eastward flow X intensity on the section 5; **(d)**, the sNECC core location on the section 5; **(e)**, the NECC intensity on the section 5; **(f)**, the sNECC core position on the section 6; and **(g)**, the NECC intensity on the section 6; **(h)**, Normalized indexes of the tropical Atlantic meridional mode (AMM: blue color) and zonal mode (AZM; black color).

668 **Table 2.** Correlations values between the characteristics of the current branches and the Atlantic meridional and

669 zonal mode indexes (AMM and AZM, respectively). Where the correlations are found lower than 0.5, we indicate

670 "insignificant" over the whole time period ("none"). The current branches analysed are the NBC (North Brazil

671 Current), sNECC (southern branch of the NECC), nSEC (the northern branch of the South Equatorial Current) and

672 the equatorial eastward flow called X.

Current branches' characteristics		Atlantic meridional mode (AMM) during March-April-May	Atlantic Zonal mode (AZM) during June-July-August
NBC1 intensity (section 1)	Correlation	Higher than -0.51	Insignificant
	Period	June-July	None
NBC2 intensity (section 1)	Correlation	0.58	Insignificant
	Period	March-April-May	None
sNECC5 intensity (section 5)	Correlation	Insignificant	-0.51
	Period	None	September
sNECC6 intensity (section 6)	Correlation	Higher than 0.50	Insignificant
	Period	March-April-May	None
sNECC6 core location (section 6)	Correlation	Higher than 0.51	Insignificant
	Period	March-April-May	None
nNECC6 core location (section 6)	Correlation	-0.62	Insignificant
	Period	March	None
nSEC5 intensity (section 5)	Correlation	Insignificant	-0.52
	Period	None	November
nSEC6 intensity (section 6)	Correlation	Higher than 0.52	Insignificant
	Period	March-April-May	None
Equatorial eastward flow X (Sections 4 and 5)	Correlation	Higher than -0.55	Insignificant
	Period	May-June	None
Equatorial eastward flow X (Section 6)	Correlation	Higher than 0.62	Higher than -0.52
	Period	March-April-May	June-July

673

674

675

676

677

678

679

680   The AMM index is found anticorrelated with the NBC intensity along the section 1 during

681   March-April-May, the nNECC core location along the section 6 and the equatorial eastward

682   flow (X) intensity west of 42° W, with respective coefficient of correlation (cc) higher than -

683   0.51 during June-July, about -0.62 in March, and higher than -0.55 in May-June. These anti-

684   correlations show the probability of the positive (negative) AMM phases to lead the negative

685   (positive) anomalies of the nNECC core location at 32° W with 0-month delay, the negative

686   (positive) NBC intensity between 3°-5° S and the X flow intensity anomalies (west of 42° W)

687   with 1- to 2-month and 0- to 1-month delay, respectively. However, the AMM index during

688   March-April-May is found correlated with the NBC intensity north of the equator before the

689   retroflection (cc ~0.58) and, the sNECC intensity/core location and the nSEC intensity at 32°

690   W (cc higer than 0.50/0.51 and cc higher than 0.52, respectively) during the same period of

691   time. This suggests that the positive (negative) AMM phases probably drives the positive

692   (negative) anomalies of the corresponding currents with no time lag.

693   During June-July-August, the AZM index is found anticorrelated with the sNECC/nSEC

694   intensity at 42° W (cc=-0.51/-0.52) only in September/November. It suggests that the positive

695   (negative) AZM phases probably lead the negative (positive) anomalies of the sNECC/nSEC

696   intensity with 1- and 3-month delay, respectively.

697   The eastward flow X intensity at 32° W is found simultaneously correlated with AZM and

698   AMM in June-July and March-April-May, with cc higher than 0.62 and -0.52, respectively.

699   This suggests that the positive (negative) anomalies of X at 32° W might be associated with

700   both positive (negative) AZM and negative (positive) AMM phases with no delay.

701   Referring to Cabos et al. (2019), the relationships found between the currents and the AMM

702   show the influence of the strengthening / weakening of the southeast trade winds in the southern

703   hemisphere on the southward / northward migration of the nNECC core at 32° W, whereas the

704   NBC intensity between 3°-5° S and the equatorial eastward flow X intensity west of 42° W

705   decrease / increase. Conversely, the strengthening / weakening of the southeast trade winds in

706   the southern hemisphere should influence the northward / southward migration of the sNECC

707   core at 32° W, whereas the NBC2, sNECC6 and nSEC6 intensities increase / decrease.

708   Referring to the same authors, the relationship with the AZM should indicate the probable

709   influence of the positive / negative westerlies anomalies in the western part of the basin on the

710   negative / positive anomalies of the sNECC and nSEC intensities at 42° W. Concerning the

711   eastward flow X at 32° W the relationship with both the AZM and the AMM modes should

712   indicate its strengthening / weakening during the concurrent events of positive / negative

27

713   westerlies anomalies in the western part of the basin and the negative / positive southerlies

714   winds anomalies in the southern hemisphere.

6   Discussion

716   Finally, we have computed the seasonal maps of the geostrophic currents in the whole WTA

717   (Fig. 8) in order to have a regional view of the seasonal variations of the circulation. Fig. 8

718   confirms the results obtained from the analysis of the cross-section velocities in Sect. 4 (in terms

719   of seasonal cycles and spatial structure) but also highlights interesting new features.

720   A large cyclonic circulation is observed between 35°-45° W and 0°-5° N during boreal spring

721   (blue ellipse). The latter is formed by the westward nSEC which is suddenly deviated to the

722   northeast by the presence of an eastward flow at ~32° W. Then, near 44° W and 5° N, the nSEC

723   meets the rNBC which reaches it southernmost position during this season, and deviates to the

724   southeast. When reaching the equatorial region between 0°-2° N, where the equatorial eastward

725   flow is found (Fig. 4), the resulting flow becomes stronger, and is deviated to the east, close

726   this cyclonic feature. This finding might answer the question of Schott et al. (1998) about the

727   destination of the rNBC during spring, when the rNBC does not feed the NECC anymore.

728   During the boreal winter, another cyclonic circulation is observed between 44°-50° W and 5°-

729   10° N (blue ellipse in Fig. 8): part of the NECC recirculates north-westward to join the rNBC.

730   During both boreal winter and spring, a south-westward recirculation of the NECC appear to

731   strengthen the nSEC located west of 32° W. It is consistent with the increase of the nSEC

732   intensity observed along section 4, compared to the nSEC intensity captured along section 6,

733   between February and May (Fig. 5b).

734   During the second half of the year, Fig. 8 shows a wider NECC which extends north of 10°N.

735   During boreal fall, the NECC flow is formed by a nNECC branch separated from the initial

736   sNECC branch during between 38°-48° W, that meet east of 38° W. This is consistent with Fig.

737   4 S5-S6. During boreal summer, the nNECC branch seems to be supplied by the northern part

738   of the NBC retroflection. This connection seems to fade during boreal fall.

739   In the equatorial region (2° S-2° N), Fig. 8 also shows an equatorial eastward flow X with lower

740   amplitude which appears to be extended east of 32° W and stronger during boreal spring and

741   fall. This feature can be related to the near-surface eastward flow mentioned by Hisard and

742   Hénin (1987) and Bourlès et al. (1999b) on top of the EUC in the WTA. Hisard and Hénin

743   (1987) explained the poor description of this current in the literature by the difficulty of ADCPs

28

744   measurements to fully capture the upper layer currents in this area. They showed that this near-

745   surface current, independent from the EUC, can reach amplitudes larger than 0.5 m s^{-1} between

746   23° W and 28° W. In order to understand this difference in current amplitude, compared to ours

747   (~ 0.1 m s^{-1}), we computed the seasonal maps of the near-surface Ekman currents (Fig. 9). We

748   observe westward currents with higher amplitudes in this equatorial band (larger than 0.2 m s^{-}

749   ^{1}). Then, we conclude that the near-surface velocities found in this study in the equatorial region

750   are underestimated, particularly in the eastern basin, compared to the absolute surface velocities

751   (Fig. 5b).

752   For the first time, the seasonal cycle of the equatorial eastward flow has been analyzed in Sect.

753   4.4 of this study (Fig. 4S4, S5, S6 and Fig. 5b). It is similar with the seasonal cycle of the EUC

754   (semi-annual cycle with two maximum), which might be due to the fact that most part of the

755   flow is fed by the rNBC.

756

757

758

759

760

761

762

763
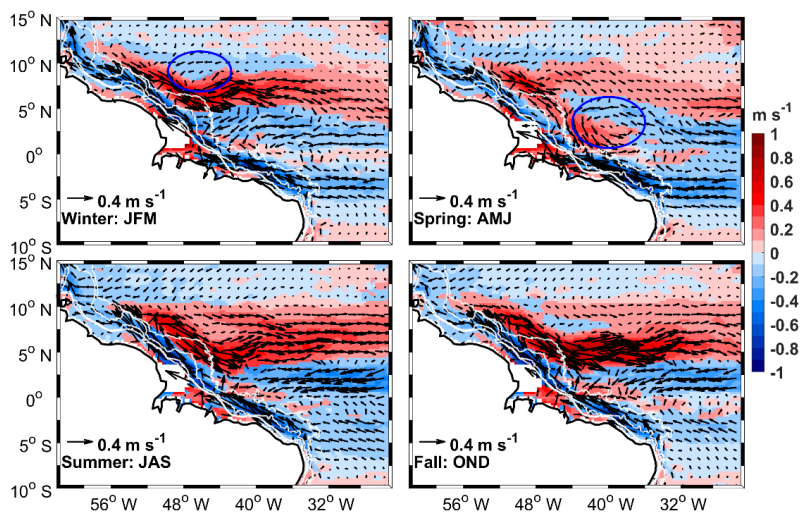
Figure 8. Seasonal maps of the geostrophic currents in the western tropical Atlantic over the 1993-2017 period for boreal winter (top left panel: JFM for January-February-March), boreal spring (top right panel: AMJ for April-May-June), boreal summer (bottom left panel: JAS for July-August-September:) and boreal fall (bottom right panel: OND for October-November-December:). The velocity vectors are superimposed on the velocity amplitudes multiplied by the sign of their horizontal components (m s^{-1}). The two cyclonic circulations observed during boreal winter and spring are indicated by blue ellipses. The white lines near to the continent are from west to east, the 300 m, 1000 m, 3000 m and 4000 m isobaths.
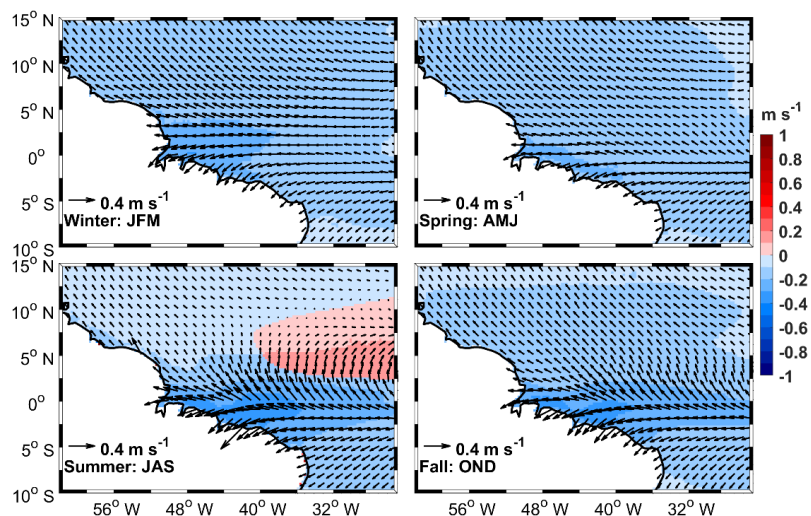
Figure 9. Seasonal maps of the Ekman currents in the western tropical Atlantic over the 1993-2017 period for boreal winter (top left panel: JFM for January-February-March:), boreal spring (top right panel: AMJ for April-May-June), boreal summer (bottom left panel: JAS for July-August-September) and boreal fall (bottom right panel: OND for October-November-December). The velocity vectors are superimposed on the velocity amplitudes multiplied by the sign of their horizontal components (m s^{-1}).

795 Finally, the current analysis made above, allows us to derive a new scheme of the seasonal

796 variations of the western boundary tropical Atlantic circulation (Fig. 10). The new current

797 branches found in this study are indicated in green and the currents coming from the north/south

798 are in blue/orange. The width of the current arrows is proportional to the current amplitude and

799 the dotted arrows represent the currents with the minimum amplitudes. C1 and C2 are for

800 respectively, the cyclonic circulations highlighted between 44°-50° W and 35°-45° W.

801

802

803

804

805

806

807

808

809

810

811

812

813
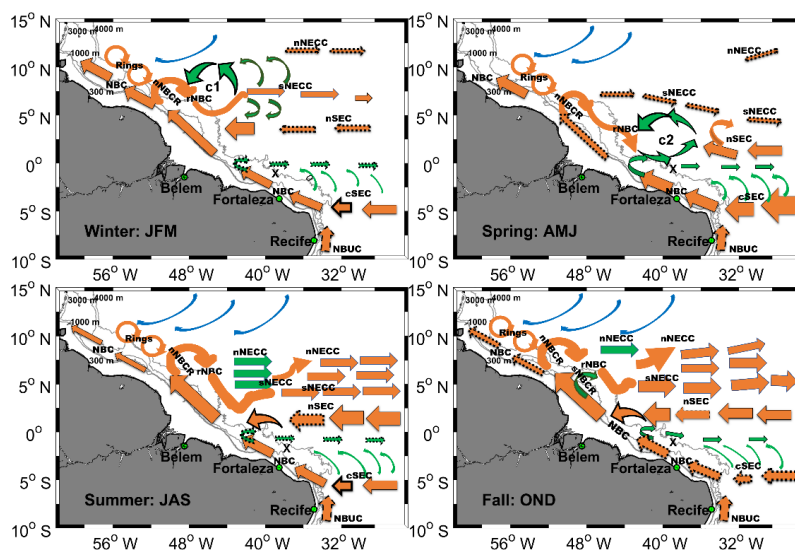
Figure 10. Schematic view of the seasonal maps of the tropical western boundary circulation. C1 and C2 represent the cyclonic circulations highlighted in this study. The wider (dotted thin) arrows show current branches with maximum (minimum) intensity. The subsurface NBUC is represented by dashed arrows. The already known current branches are in orange/blue. The green arrows characterize the new branches observed. NBC is the North Brazil Current; nNBCR and sNBCR are the northern and the southern flows of the North Brazil Current retroflection, respectively; rNBC is the retroflected branch of North Brazil current; nNECC and sNECC are the northern and the southern branches of the North Equatorial Countercurrent (NECC), respectively; cSEC and nSEC are the central and the northern branches of the South Equatorial Current (SEC), respectively.

834 Concerning the interannual variability, Hormann et al. (2012), based on the analyses of 17 year

835 of altimetry and drifter' data, found interesting scenarios about the NECC spatial and temporal

836 variability. However, they did not separate the sNECC from the nNECC. In their study, the

837 authors have associated the strengthening of the NECC in the whole basin to the negative phase

838 of the AZM, and its northward shift to the positive phase of the AMM. Our results show

839 different behaviors of the NECC system as a function of the branch and core location. We also

840 showed possible relationships between the southern NECC branch intensity and location with

841 the AMM phases at 42° W, and conversely a possible relationship between the southern NECC

842 branch intensity and location with the AZM phases at 32° W. These results open the way to

843 deeper investigations in future studies.

844 **7   Summary and Perspectives**

845 Twenty-five years (1993-2017) of gridded altimetry data from CMEMS were used to improve

846 the description of the seasonal and interannual variations of the western boundary circulation

847 of the tropical Atlantic. Therefore, we defined six horizontal sections crossing the main upper

848 layer currents' veins. C3S ERA5 wind estimates and the NOAA OI SST v2 product were also

849 used to investigate the possible link between the variability of the regional circulation and the

850 large-scale remote wind forcing on one hand, and the tropical Atlantic climate modes on the

851 other hand.

852 Our results highlight a complex regional circulation, with significant seasonal and year-to-year

853 variations of the currents' intensity and location. South of the equator, we observe a

854 stronger/weaker central branch of the South Equatorial Atlantic (cSEC) and of the North Brazil

855 Current (NBC) during boreal spring/fall. North of the equator, the NBC component flowing

856 along the Guyana coast exhibits a similar annual cycle. However, between both, the NBC part

857 located before the retroflection is out of phase (i.e. stronger during summer-fall), when fed by

858 the northern branch of the South Equatorial Current (nSEC). Its larger amplitudes appear during

859 boreal fall, 3-4 months after the maximum of the remote wind stress curl (WSC) strength (in

860 August). The North Equatorial Countercurrent (NECC) is connected with the retroflected

861 branch of the NBC, and both show similar annual cycle. A secondary North Brazil Current

862 Retroflection (NBCR) was observed for the first time during boreal fall in this study: it is

863 located between 4°-6° N. The two-core/branch structure of the NECC during the second half of

864 the year was also confirmed and analyzed separately. Between 0°-5° N and 35°-45° W, a surface

865 cyclonic circulation develops during boreal spring. It is found to initiate the growth of the

NECC at 42° W in June. However, at 32° W, the NECC doesn't show any connection with this cyclonic circulation, but starts its seasonal cycle earlier in April when the ITCZ migrates northward and the remote WSC strengthens. In the equatorial region, between 2° S-2° N, the geostrophic currents show the presence of an equatorial surface eastward flow which has a seasonal cycle similar to the Equatorial Undercurrent (EUC). But he near-surface Ekman currents have to be taken into account here to have a good description of the surface circulation.

Concerning the interannual variability, it is much weaker than the seasonal one. We do not observe an obvious picture at regional scale but it is more important in the eastern part of the basin. The analysis of the changes in characteristics of the different current branches (intensity and core location), with respect to the tropical Atlantic climate modes, shows different possible scenarios associated with one or both modes. It opens the way to further investigations concerning the link between the Atlantic climate modes (ACM) and the current transports, not possible with altimetry alone.

As a conclusion, this study demonstrates the ability of altimetry to characterize the seasonal and interannual variability of the surface circulation in the study area. It confirm previous findings but also significantly complements the knowledge of the different currents at regional scale. Combined use of regional modelling, altimetry and in-situ observations will allow to go further in the understanding of the spatial and temporal structure of the regional circulation. The intraseasonal variability, significant in the near-shore region of the study area (Fig. 2d) is not studied here. It will be the subject of a future work, based on a coastal altimetry product that will allow a significantly better resolution and accuracy along the continental shelf, compared to a gridded product.

Authors contribution

Djoirka M. Dimoune performed the data analyses as part of his PhD thesis. Florence Birol, Fabrice Hernandez, Fabien Leger and Moacyr Araujo supervised this research.

Competing interests

The authors declare that they have no conflict of interest.

Acknowledgements

References

Aguedjou, H. M. A., Dadou, I., Chaigneau, A., Morel, Y., and Alory, G.: Eddies in the Tropical Atlantic Ocean and their seasonal variability, Geophys. Res. Lett., *46*(21), 12156-12164, https://doi.org/10.1029/2019GL083925, 2019.

Araujo, M., Noriega, C., Hounsou-Gbo, G. A., Veleda, D., Araujo, J., Bruto, L., Feitosa, F., Flores-Montes, M., Lefèvre, N., Melo, P., Ostuska, A., Travassos, K., Schwamborn, R., Neumann-Leitão, S.: A synoptic assessment of the amazon river-ocean continuum during boreal autumn: From physics to plankton communities and carbon flux, Front. Microbiol., 8, 1358, https://doi.org/10.3389/fmicb.2017.01358, 2017.

Arbic, B. K., Scott, R. B., Chelton, D. B., Richman, J. G., and Shriver, J. F.: Effects of stencil width on surface ocean geostrophic velocity and vorticity estimation from gridded satellite altimeter data, J. Geophys. Res.-Oceans, 117(C3), https://doi.org/10.1029/2011jc007367, 2012.

Aroucha, L. C., Veleda, D., Lopes, F. S., Tyaquiçã, P., Lefèvre, N., and Araujo, M.: Intra-and Inter-Annual Variability of North Brazil Current Rings Using Angular Momentum Eddy

923   Detection and Tracking Algorithm: Observations From 1993 to 2016, J. Geophys. Res.-

924   Oceans, 125(12), e2019JC015921, https://doi.org/10.1029/2019jc015921, 2020.

925   Burmeister K., Lübbecke, J. F.,Brandt, P., and Duteil, O.: Interannual variability of the

926   Atlantic North Equatorial Undercurrent and its impact on oxygen, J. Geophys. Res.-Oceans,

927   124, 2348–2373, https://doi.org/10.1029/2018JC014760, 2019.

928   Bourles, B., Molinari, R. L., Johns, E., Wilson, W. D., and Leaman, K. D.: Upper layer

929   currents in the western tropical North Atlantic (1989–1991), J. Geophys. Res.-Oceans,

930   104(C1), 1361-1375, https://doi.org/10.1029/1998jc9000250, 1999.

931   Bourlès, B., Gouriou, Y., and Chuchla, R.: On the circulation in the upper layer of the western

932   equatorial Atlantic, J. Geophys. Res.-Oceans, 104(C9), 21151-21170,

933   https://doi.org/10.1029/1999jc900058, 1999.

934   Brandt, P., Schott, F. A., Provost, C., Kartavtseff, A., Hormann, V., Bourlès, B., and Fischer,

935   J.: Circulation in the central equatorial Atlantic: Mean and intraseasonal to seasonal

936   variability, Geophys. Res. Lett., 33(7), https://doi.org/10.1029/2005gl025498, 2006.

937   Brandt, P., Claus, M., Greatbatch, R. J., Kopte, R., Toole, J. M., Johns, W. E., and Böning, C.

938   W.: Annual and semiannual cycle of equatorial Atlantic circulation associated with basin-

939   mode resonance, J. Phys. Oceanogr., 46(10), 3011-3029, https://doi.org/10.1175/jpo-d-15-

940   0248.1, 2016.

941   Cabos, W., de la Vara, A., and Koseki, S.: Tropical Atlantic variability: observations and

942   modelling, Atmosphere, 10(9), 502, https://doi.org/10.3390/atmos10090502, 2019.

943   Cochrane, J. D., Kelly Jr, F. J., and Olling, C. R.: Subthermocline countercurrents in the

944   western equatorial Atlantic Ocean, J. Phys. Oceanogr., 9(4), 724-738,

945   https://doi.org/10.1175/1520-0485(1979)009<0724:scitwe>2.0.co;2, 1979.

946   Didden, N., and Schott, F.: Seasonal variations in the western tropical Atlantic: Surface

947   circulation from Geosat altimetry and WOCE model results, J. Geophys. Res.-Oceans,

948   97(C3), 3529-3541, https://doi.org/10.1029/91jc02860, 1992.

949   Dossa, A. N., Silva, A. C., Chaigneau, A., Eldin, G., Araujo, M., and Bertrand, A.: Near-

950   surface western boundary circulation off Northeast Brazil, Prog. Oceanogr., 190, 102475,

951   https://doi.org/10.1016/j.pocean.2020.102475, 2021.

952 Ffield, A.: North Brazil current rings viewed by TRMM Microwave Imager SST and the

953 influence of the Amazon Plume, Deep-Sea Res. Pt. I, 52(1), 137-160,

954 https://doi.org/10.1016/j.dsr.2004.05.013, 2005.

955 Fonseca, C. A., Goni, G. J., Johns, W. E., and Campos, E. J.: Investigation of the north Brazil

956 current retroflection and north equatorial countercurrent variability, Geophys. Res. Lett.,

957 31(21), https://doi.org/10.1029/2004gl020054, 2004.

958 Fratantoni, D. M., Johns, W. E., Townsend, T. L., and Hurlburt, H. E.: Low-latitude

959 circulation and mass transport pathways in a model of the tropical Atlantic Ocean, J. Phys.

960 Oceanogr., 30(8), 1944-1966,

961 https://doi.org/10.1175/15200485(2000)030<1944:LLCAMT>2.0.CO;2, 2000.

962 Garzoli, S. L., and Katz, E. J.: The forced annual reversal of the Atlantic North Equatorial

963 Countercurrent, J. Phys. Oceanogr., 13(11), 2082-2090, https://doi.org/10.1175/1520-

964 0485(1983)013<2082:tfarot>2.0.co;2, 1983.

965 Garzoli, S. L.: The Atlantic North Equatorial Countercurrent: Models and observations, J.

966 Geophys. Res.-Oceans, 97 (C11), 17931-17946, https://doi.org/10.1029/92jc01363, 1992.

967 Garzoli, S. L., Ffield, A., and Yao, Q.: North Brazil Current rings and the variability in the

968 latitude of retroflection, Elsevier Oceanogr. Ser., 68, 357-373, https://doi.org/10.1016/s0422-

969 9894(03)80154-x, 2003.

970 Garzoli, S. L., Ffield, A., Johns, W. E., and Yao, Q.: North Brazil Current retroflection and

971 transports, J. Geophys. Res.-Oceans, 109(C1), https://doi.org/10.1029/2003jc001775, 2004.

972 Garzoli, S. L., and Matano, R.: The South Atlantic and the Atlantic meridional overturning

973 circulation, Deep-Sea Res. II, 58(17-18), 1837-1847,

974 https://doi.org/10.1016/j.dsr2.2010.10.063, 2011.

975 Gill, A. E., and Adrian, E.: Atmosphere-ocean dynamics, Vol. 30, Academic press,

976 https://doi.org/10.1016/s0074-6142(08)60025-x, 1982.

977 Góes, M., and Wainer, I.: Equatorial currents transport changes for extreme warm and cold

978 events in the Atlantic Ocean, Geophys. Res. Lett., 30(5),

979 https://doi.org/10.1029/2002gl015707, 2003.

980 Goes, M., Molinari, R., da Silveira, I., and Wainer, I.: Retroflections of the north brazil

981 current during february 2002, Deep-Sea Res. Pt. I, *52*(4), 647-667,

982 https://doi.org/10.1016/j.dsr.2004.10.010, 2005.

983 Goni, G. J., and Johns, W. E.: Synoptic study of warm rings in the North Brazil Current

984 retroflection region using satellite altimetry, Elsevier Oceanogr. Ser., 68, 335-356,

985 https://doi.org/10.1016/s0422-9894(03)80153-8, 2003.

986 Hazeleger, W., and De Vries, P.: Fate of the Equatorial Undercurrent in the Atlantic, Elsevier

987 Oceanogr. Ser., 68, 175-191, https://doi.org/10.1016/s0422-9894(03)80146-0, 2003.

988 Hazeleger, W., de Vries, P., and Friocourt, Y.: Sources of the Equatorial Undercurrent in the

989 Atlantic in a high-resolution ocean model, J. Phys. Oceanogr., 33(4), 677-693,

990 https://doi.org/10.1175/1520-0485(2003)33<677:soteui>2.0.co;2, 2003.

991 Hisard, P., and Hénin, C.: Response of the equatorial Atlantic Ocean to the 1983–1984 wind

992 from the Programme Français Océan et Climat dans l'Atlantique Equatorial cruise data set, J.

993 Geophys. Res.-Oceans, 92(C4), 3759-3768, https://doi.org/10.1029/jc092ic04p03759, 1987.

994 Hormann, V., and Brandt, P.: Atlantic Equatorial Undercurrent and associated cold tongue

995 variability, J. Geophys. Res.-Oceans, 112(C6), https://doi.org/10.1029/2006jc003931, 2007.

996 Hormann, V., Lumpkin, R., and Foltz, G. R.: Interannual North Equatorial Countercurrent

997 variability and its relation to tropical Atlantic climate modes, J. Geophys. Res.-Oceans,

998 117(C4), https://doi.org/10.1029/2011jc007697, 2012.

999 Jochum, M., and Malanotte-Rizzoli, P.: On the generation of North Brazil Current rings, J.

1000 Mar. Res., 61(2), 147-173, https://doi.org/10.1357/002224003322005050, 2003.

1001 Johns, W. E., Lee, T. N., Schott, F. A., Zantopp, R. J., and Evans, R. H.: The North Brazil

1002 Current retroflection: Seasonal structure and eddy variability, J. Geophys. Res.-Oceans,

1003 95(C12), 22103-22120, https://doi.org/10.1029/jc095ic12p22103, 1990.

1004 Johns, W. E., Lee, T. N., Beardsley, R. C., Candela, J., Limeburner, R., and Castro, B.:

1005 Annual cycle and variability of the North Brazil Current, J. Phys. Oceanogr., *28*(1), 103-128,

1006 https://doi.org/10.1175/1520-0485(1998)028<0103:acavot>2.0.co;2, 1998.

1007 Lagerloef, G. S., Mitchum, G. T., Lukas, R. B., and Niiler, P. P.: Tropical Pacific near-surface

1008 currents estimated from altimeter, wind, and drifter data, J. Geophys. Res.-Oceans, 104(C10),

1009 23313-23326, https://doi.org/10.1029/1999jc900197, 1999.

1010 Large, W. G., and Pond, S.: Open ocean momentum flux measurements in moderate to strong

1011 winds, J. Phys. Oceanogr., 11(3), 324-336, https://doi.org/10.1175/1520-

1012 0485(1981)011<0324:oomfmi>2.0.co;2, 1981.

1013 NRSC: OSCAT Wind stress and Wind stress curl products, Ocean Sciences Group, Earth and

1014 Climate Science Area, Hyderabad, India, 18 pp., 2013.

1015 Peterson, R. G., and Stramma, L.: Upper-level circulation in the South Atlantic Ocean, Prog.

1016 Oceanogr., 26(1), 1-73, https://doi.org/10.1016/0079-6611(91)90006-8, 1991.

1017 Provost, C., Arnault, S., Chouaib, N., Kartavtseff, A., Bunge, L., and Sultan, E.:

1018 TOPEX/Poseidon and Jason equatorial sea surface slope anomaly in the Atlantic in 2002:

1019 Comparison with wind and current measurements at 23W, Mar. Geod., 27(1-2), 31-45,

1020 https://doi.org/10.1080/01490410490465274, 2004.

1021 Pujol, M. I., Faugère, Y., Taburet, G., Dupuy, S., Pelloquin, C., Ablain, M., and Picot, N.:

1022 DUACS DT2014: the new multi-mission altimeter data set reprocessed over 20 years, Ocean

1023 Sci., 12(5), 1067-1090, https://doi.org/10.5194/os-2015-110, 2016.

1024 Richardson, P. L., and Walsh, D.: Mapping climatological seasonal variations of surface

1025 currents in the tropical Atlantic using ship drifts, J. Geophys. Res.-Oceans, 91(C9), 10537-

1026 10550, https://doi.org/10.1029/jc091ic09p10537, 1986.

1027 Rodrigues, R. R., Rothstein, L. M., and Wimbush, M.: Seasonal variability of the South

1028 Equatorial Current bifurcation in the Atlantic Ocean: A numerical study, J. Phys. Oceanogr.,

1029 37(1), 16-30, https://doi.org/10.1175/jpo2983.1, 2007.

1030 Schmitz Jr, W. J., and McCartney, M. S.: On the north Atlantic circulation, Rev. Geophys.,

1031 31(1), 29-49, https://doi.org/10.1029/92RG02583, 1993.

1032 Schott, F. A., Stramma, L., and Fischer, J.: The warm water inflow into the western tropical

1033 Atlantic boundary regime, spring 1994, J. Geophys. Res.-Oceans, 100(C12), 24745-24760,

1034 https://doi.org/10.1029/95jc02803, 1995.

1035 Schott, F. A., Fischer, J., and Stramma, L.: Transports and pathways of the upper-layer

1036 circulation in the western tropical Atlantic, J. Phys. Oceanogr., 28(10), 1904-1928,

1037 https://doi.org/10.1175/1520-0485(1998)028<1904:tapotu>2.0.co;2, 1998.

1038 Schott, F. A., McCreary Jr, J. P., and Johnson, G. C.: Shallow overturning circulations of the
1039 tropical-subtropical oceans, Washington DC American Geophysical Union Geophys. Monogr.
1040 Ser., 147, 261-304, https://doi.org/10.1029/147gm15, 2004.

1041 Servain, J.: Simple climatic indices for the tropical Atlantic Ocean and some applications, J.
1042 Geophys. Res.-Oceans, 96 (C8), 15137-15146, https://doi.org/10.1029/91jc01046, 1991.

1043 Silva, M., Araujo, M., Servain, J., Penven, P., and Lentini, C. A.: High-resolution regional
1044 ocean dynamics simulation in the southwestern tropical Atlantic. Ocean Model., 30(4), 256-
1045 269, https://doi.org/10.1016/j.ocemod.2009.07.002, 2009.

1046 Stramma, L., and Schott, F.: The mean flow field of the tropical Atlantic Ocean, Deep-Sea
1047 Res. Pt. II, 46(1-2), 279-303, https://doi.org/10.1016/s0967-0645(98)00109-x, 1999.

1048 Stramma, L., and England, M.: On the water masses and mean circulation of the South
1049 Atlantic Ocean, J. Geophys. Res.-Oceans, 104(C9), 20863-20883,
1050 https://doi.org/10.1029/1999JC900139, 1999.

1051 Sudre, J., Maes, C., and Garçon, V.: On the global estimates of geostrophic and Ekman
1052 surface currents, Limnol. Oceanogr.: Fluids Environ., 3(1), 1-20,
1053 https://doi.org/10.1215/21573689-2071927, 2013.

1054 Trenberth, K. E., Large, W. G., and Olson, J. G.: The mean annual cycle in global ocean wind
1055 stress, J. Phys. Oceanogr., 20(11), 1742-1760, https://doi.org/10.1175/1520-
1056 0485(1990)020<1742:TMACIG>2.0.CO;2, 1990.

1057 Urbano, D. F., Jochum, M., and Da Silveira, I. C. A.: Rediscovering the second core of the
1058 Atlantic NECC, Ocean model., 12(1-2), 1-15, https://doi.org/10.1016/j.ocemod.2005.04.003,
1059 2006.

1060 Urbano, D. F., De Almeida, R. A. F., and Nobre, P.: Equatorial Undercurrent and North
1061 Equatorial Countercurrent at 38 W: A new perspective from direct velocity data, J. Geophys.
1062 Res.-Oceans, 113(C4), https://doi.org/10.1029/2007jc004215, 2008.

1063 Verdy, A., and Jochum, M.: A note on the validity of the Sverdrup balance in the Atlantic
1064 North Equatorial Countercurrent, Deep-Sea Res. Pt. I, 52(1), 179-188,
1065 https://doi.org/10.1016/j.dsr.2004.05.014, 2005.

1066 Zebiak, S. E.: Air–Sea Interaction in the Equatorial Atlantic Region, J. Clim., 6 (8), 1567-
1067 1586, https://doi.org/10.1175/1520-0442(1993)006<1567:AIITEA>2.0.CO;2, 1993.

1068   Zheng, Y., and Giese, B. S.: Ocean heat transport in simple ocean data assimilation: Structure

1069   and mechanisms, J. Geophys. Res.-Oceans, 114(C11), https://doi.org/10.1029/2008jc005190,

1070   2009.